



Synthesis of hierarchical and bridging carbon-coated $\text{LiMn}_{0.9}\text{Fe}_{0.1}\text{PO}_4$ nanostructure as cathode material with improved performance for lithium ion battery

Feng Ma^{a,1}, Xiaoyu Zhang^{a,1}, Ping He^{a,*}, Xueping Zhang^a, Peng Wang^b,
Haoshen Zhou^{a,c,**}

^a Center of Energy Storage Materials & Technology, College of Engineering and Applied Sciences, National Laboratory of Solid State Microstructures, Collaborative Innovation Center of Advanced Microstructures, Nanjing University, Nanjing 210093, PR China

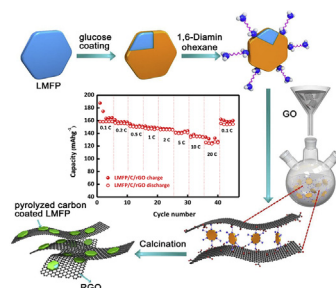
^b Department of Materials Science and Engineering, College of Engineering and Applied Sciences, Nanjing University, Nanjing 210093, PR China

^c Energy Technology Research Institute, National Institute of Advanced Industrial Science and Technology, Umezono 1-1-1, Tsukuba, 305-8568, Japan

HIGHLIGHTS

- LMFP nanoplate with hierarchical and bridging carbon-coating are synthesized.
- A simple amine-assisted carbon coating strategy is proposed.
- The electronic and ionic conductivity is greatly improved by the coating strategy.
- LMFP nanoplate exhibits superior rate performance and long-term cycling stability.

GRAPHICAL ABSTRACT



ARTICLE INFO

Article history:

Received 23 December 2016

Received in revised form

17 May 2017

Accepted 19 May 2017

Available online 3 June 2017

Keywords:

Li-ion battery

Rate capability

$\text{LiMn}_{0.9}\text{Fe}_{0.1}\text{PO}_4$

Graphene

Carbon-coating strategy

ABSTRACT

A pyrolyzed carbon and reduced graphene oxide co-doped $\text{LiMn}_{0.9}\text{Fe}_{0.1}\text{PO}_4$ (LMFP/C/rGO) is synthesized by a novel and facile amine-assisted coating strategy. The well designed co-doped $\text{LiMn}_{0.9}\text{Fe}_{0.1}\text{PO}_4$ nanoplate (LMFP/C/rGO, 150 nm in length and 20 nm in thickness) is proved to be olivine phase with good crystallinity which is further compared with the sole pyrolyzed carbon coated $\text{LiMn}_{0.9}\text{Fe}_{0.1}\text{PO}_4$ (LMFP/C) from structural and electrochemical points of views. The LMFP/C/rGO exhibits superior electrochemical performances with the specific capacity of 158.0 mAh g^{-1} at 0.1C and 124.6 mAh g^{-1} at 20C, which is, to the best of our knowledge, the highest rate capability. Moreover, after 140 cycles at 0.2C rate, around 95% of the initial capacity is still retained. Further analyses disclosed the outstanding electrochemical performances can be ascribed to the collaboration of the uniformly coated pyrolyzed carbon and closely connected rGO with an extraordinary electronic conductivity. Our research shows this effective synthesis strategy is imperative for the improvement of Li-ion battery performance and can be widely used for advanced energy storage.

© 2017 Published by Elsevier B.V.

* Corresponding author.

** Corresponding author. Center of Energy Storage Materials & Technology, College of Engineering and Applied Sciences, National Laboratory of Solid State Microstructures, Collaborative Innovation Center of Advanced Microstructures, Nanjing University, Nanjing 210093, PR China.

E-mail addresses: pinghe@nju.edu.cn (P. He), hs.zhou@aist.go.jp (H. Zhou).

¹ These authors contributed equally to this work.

1. Introduction

Nowadays, with the increasing concern of the energy resources and environmental issues, a lot of efforts have been made of using the renewable energy resources in order to release the dependence of mines, fossil fuels consumption and alleviate the global warming, climate change causing from the gas emission. Among those efforts, lithium-ion battery, which has been successfully used in the portable electronic devices, is promising for the electric and plug-in hybrid vehicles and expected to be the key technology for the future renewable energy storage and conversion system.

The energy and power density of Li-ion battery is largely determined by the cathode materials. Among lots of candidate for the cathode materials, olivine-structured lithium transition metal phosphates LMPO_4 ($M = \text{Mn, Fe, Co, Ni}$), especially LiFePO_4 (LFP), draws continuously research interested ever after its first introduced by Goodenough et al., in 1997 [1] based on its thermal stability, low cost and environment benignity [2–5]. However, the relative low working voltage of LiFePO_4 , 3.45 V vs. Li/Li^+ , hinders its further application towards the higher energy density device and the larger scale energy storage system. As one of the potential alternative materials of LiFePO_4 , olivine structure LiMnPO_4 (LMP) with the $\text{Mn}^{2+/3+}$ redox couple has a higher operating voltage (4.1 V vs. Li/Li^+) compared with LiFePO_4 with the $\text{Fe}^{2+/3+}$ redox (3.45 V vs. Li/Li^+) [3,6,7]. This high electrochemical potential of LMP falls within the stability windows of commonly used electrolyte which meets the thermodynamic requirements of the Li-ion battery upon cycling [8]. Meanwhile, collaborated with some graphite anode, the specific energy density of the battery with the cathode material of LiMnPO_4 is 456 Wh kg^{-1} which is higher than the LiFePO_4 (390 Wh kg^{-1}) cathode system [9,10]. Nonetheless, LiMnPO_4 still suffers some drawbacks especially of its inherent poor electric (10^{-11} – 10^{-8} S cm^{-1}) and ionic conductivity (10^{-9} – 10^{-7} $\text{cm}^{-2}\text{s}^{-1}$) which are the hurdles of its practical using [11,12]. The Jahn-Teller effect originating from $\text{Mn}^{2+/3+}$ is another issue of using LiMnPO_4 as the cathode material for practical Li-ion battery. This effect would lead to the meta-stability of the delithiated phase and the drastic capacity degradation compared with LiFePO_4 [13–15].

Aiming to improve the electrochemical performance of LiMnPO_4 , considering efforts have been made such as nanosizing, cation doping, carbon coating and so on. The size reduction results in a reduced diffusion distance for electrons and Li-ions which enhances the kinetics for Li-ion uptake and enables improved capacity retention and high rate cycling capability [16–19]. Doping of two-valence cations such as Co^{2+} , Mg^{2+} , Fe^{2+} , etc. [20–23] has been explored to alleviate the Jahn-Teller distortion, among which $\text{LiMn}_{1-x}\text{Fe}_x\text{PO}_4$ (x from 0 to 1) has attracted intensive attention as it exhibits relative higher energy and power density inherited from LMP and LFP, respectively [24–27].

The approach of coating conductive carbon is the most common used strategy to address the low electronic and ionic conductivity for LiMnPO_4 -based olivine structure materials. The carbon used in these composite can be divided into two types. One is pyrolysed carbon, amorphous carbon, that usually arisen from organic sources such as sucrose [6,19], polymers like polymethylmethacrylate [3] and polyaniline [28]. The other is graphitic carbon such as carbon nanotube [29], vapor grown carbon fiber [30] and graphene etc. [25,31,32]. By using pyrolysed carbon, a uniform coating layer on the surface of nanoparticles is easy to achieved which provides amounts of free access for Li-ion [3,19]. However, the pyrolysed carbon always shows less electronic conductivity compared with that of graphitic carbon. Graphene with a superior electronic conductivity, has been used to modify olivine materials by ball milling method [31] or adding graphene oxide directly into the

solvothermal reactants [32]. Yet, most of the graphene carbon coating suffered a contact problem with the active material [34], therefore the advantage of using graphene can no longer be fully realized as expected. Moreover, it is still a big challenge to grow olivine phosphate materials on the graphene via solvothermal process.

In this work, we design a novel multilayer carbon coating strategy involving both the amorphous carbon and the reduced graphene oxide (rGO) to modify $\text{LiMn}_{0.9}\text{Fe}_{0.1}\text{PO}_4$ nanocrystals material as a potential high power density cathode material. The hybrid carbon source combined advantages from amorphous carbon and the graphitic carbon. With the assistance of a new bridging agent (Hexamethylene diamine), the amorphous carbon coated $\text{LiMn}_{0.9}\text{Fe}_{0.1}\text{PO}_4$ nanoparticles were strongly connected to the graphene which provide an electronic highway for the system. Our results show the uniform coating of amorphous carbon along with the high electronic conductivity rGO on the $\text{LiMn}_{0.9}\text{Fe}_{0.1}\text{PO}_4$ (LMFP/C/rGO) exhibited an excellent rate performance and good cycling stability.

2. Experimental section

2.1. Preparation of materials

2.1.1. Synthesis of $\text{LiMn}_{0.9}\text{Fe}_{0.1}\text{PO}_4$ nanocrystals(LMFP)

$\text{LiMn}_{0.9}\text{Fe}_{0.1}\text{PO}_4$ nanocrystals were synthesized using $\text{LiOH}\cdot\text{H}_2\text{O}$, MnSO_4 , FeSO_4 , H_3PO_4 and ascorbic acid as starting materials. 30 mmol of $\text{LiOH}\cdot\text{H}_2\text{O}$ dissolved in 40 mL ethylene glycol under mild heating (around 50 °C) was slowly introduced into the stirring H_3PO_4 ethylene glycol solution containing 10 mmol H_3PO_4 and 20 mL ethylene glycol. The white precipitates gradually appeared and finally became the white suspension. Subsequently, 9 mmol MnSO_4 , 1 mmol FeSO_4 and 0.6 g ascorbic acid dissolved in a mixed solvent of 35 mL ethylene glycol and 5 mL deionized water were added to the suspension with the mechanical stirring of 400 r/min. After stirring for 30 min, the final mixture was transferred into autoclaves and underwent the solvothermal process for 10 h at 180 °C.

2.1.2. Synthesis of carbon coated $\text{LiMn}_{0.9}\text{Fe}_{0.1}\text{PO}_4$ nanocrystals(LMFP/C)

$\text{LiMn}_{0.9}\text{Fe}_{0.1}\text{PO}_4$ nanocrystals and glucose were mixed with a mass ratio of 4:1 and the mixture was transferred into a tube furnace and heated at 600 °C under flowing H_2/Ar (H_2/Ar 95:5).

2.1.3. Synthesis of carbon coated $\text{LiMn}_{0.9}\text{Fe}_{0.1}\text{PO}_4$ nanocrystals/rGO composite (LMFP/C/rGO)

Graphene oxide(GO) was prepared by a modified Hummers' method [25,31,32]. Typically, 50 mL concentrated sulfuric acid (98 wt%) was slowly added to a flask with 2 g of natural graphite and 0.5 g of NaNO_3 within half an hour with a gentle stirring under an ice-bath condition (the temperature kept below 4 °C). 14 g of KMnO_4 was continuously added to that slurry within 1 h and kept stirring for 2 h. After that 200 mL of deionized water and 10 mL of H_2O_2 aqueous solution (20 wt%) were added to the thick paste respectively with the stirring speed around 400 r/min. After cooling to room temperature the prepared suspension was washed with de-ionized water until the filtrate pH value closed to 7. The obtained solid was dispersed in water again with the help of sonication to form a GO solution with a certain concentration.

$\text{LiMn}_{0.9}\text{Fe}_{0.1}\text{PO}_4$ nanocrystals and glucose were mixed with a mass ratio of 4:1 and the mixture was transferred into a tube furnace and heated at 200 °C under flowing H_2/Ar (H_2/Ar 95:5). One gram of the obtained powders were dispersed in the 200 mL absolute ethanol via sonication and then heated to 60 °C in the water

bath. To this $\text{LiMn}_{0.9}\text{Fe}_{0.1}\text{PO}_4$ dispersion, 1 g of hexamethylenediamine dissolved in 50 mL ethanol was dropped with vigorous stirring. After adding hexamethylenediamine solution completely, kept stirring for 1 h. The hexamethylenediamine modified $\text{LiMn}_{0.9}\text{Fe}_{0.1}\text{PO}_4$ was collected via centrifugation and successively rinsed with ethanol and dispersed in ethanol. The suspension was heated to 60 °C and GO suspension (containing 10 mg GO) was slowly added into this suspension with vigorous stirring. After mixing for 2 h, the mixture was then centrifuged and washed with ethanol. After dried at 60 °C, the powders were put into a 10 mL bottle which was further placed on an autoclave containing 10 mL hydrazine monohydrate and heated at 120 °C for 3 h. This process was carefully operated in order to prevent direct contact between powders and hydrazine monohydrate. After thoroughly washed with ethanol, dried under vacuum at 60 °C overnight, the powders were finally annealed at 600 °C for 4 h in H_2/Ar (5:95 vol) atmosphere.

2.2. Characterization of materials

X-ray diffraction (XRD) patterns were collected using the Bruker D8-Advanced X-ray diffractometer with $\text{Cu K}\alpha$ radiation ($\lambda = 1.5406 \text{ \AA}$) at a scan rate of 2° per minute over the 2θ range of 10–90°. Fourier Transform infrared Spectroscopy (FT-IR, Nexus 870) was used to analyze the precursors of the composite material over the wave number ranging in 4000 cm^{-1} to 400 cm^{-1} . Morphology and microstructure observations were performed using a field-emission scanning electron microscope (FESEM, SU8010, Hitachi) and a high-resolution transmission electron microscope (HRTEM, JEOL JEM–2010F). Low-temperature nitrogen adsorption–desorption isotherms and pore-size distributions were measured at –196 °C using a surface area and porosity analyzer (Micromeritics ASAP 2020, USA).

2.3. Coin-type cells assembly and electrochemical tests

Working electrodes were fabricated by mixing the active material (LMFP/C or LMFP/C/rGO), acetylene black conductive agent and polyvinylidene fluoride (PVDF) binder in the weight ratio of 80:10:10 with a few drops of *N*-methyl pyrrolidone (NMP) followed by coating the mixed slurry onto an aluminium foil current collector and dried at 100 °C for 12 h in vacuum. CR2032 coin cells were assembled in an argon filled glovebox (MIKROUNA Super 1220/750, Mikrouna (China) Co., Ltd., with O_2 and H_2O concentration <1 ppm) using the fabricated working electrodes (with the active material mass loading of *ca.* 1.5 mg), metallic lithium foil electrode, Celgard 2500 separator, and 1 M LiPF_6 dissolved in a mixture of ethylene carbonate (EC), dimethyl carbonate (DMC) and diethyl carbonate (DEC) (1:1:1, v/v/v) as electrolyte. Cyclic voltammetry (CV) and electrochemical impedance spectroscopy (EIS) measurements were performed on CHI Electrochemical Workstation (CHI 660C). Galvanostatic charge/discharge tests were carried out on Land CT2001A autocyler (China). All the electrochemical measurements were conducted at ambient temperature.

3. Results and discussion

The schematic depiction of the synthesis process for LMFP/C/rGO sample is displayed in Fig. 1 with the detail description in the Experimental Section. In general, the $\text{LiMn}_{0.9}\text{Fe}_{0.1}\text{PO}_4$ nanoparticles were first prepared by the solvothermal route. Ascorbic acid was used as the antioxidant and morphology controlling agent. From the SEM figure (Fig. S1) it can be seen, the thickness of un-coated LMFP particle is around 50 nm which is two times thicker than carbon coated LMFP (around 20 nm). Moreover, significant agglomerate was found for un-coated LMFP. Our experiment

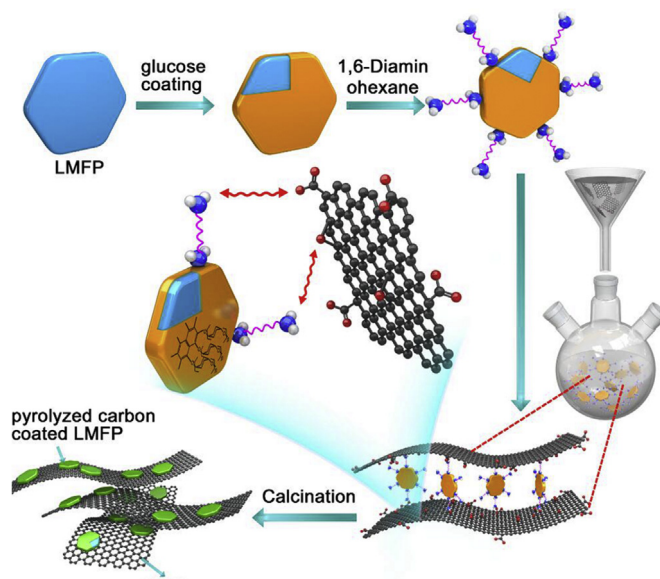


Fig. 1. Schematic representation of the synthesis process for LMFP/C/rGO.

showed the using of rational amount of ascorbic acid during the solvothermal process would effectively reduce the particle size of $\text{LiMn}_{0.9}\text{Fe}_{0.1}\text{PO}_4$ compared to the production without ascorbic acid additive.

After the solvothermal synthesis process $\text{LiMn}_{0.9}\text{Fe}_{0.1}\text{PO}_4$ nanoparticles was successfully obtained and subsequently mixed with a certain amount of glucose. Upon heat at 200 °C (higher than the melting point of glucose, 146 °C) the glucose first melted and then diffused into the interval space of the $\text{LiMn}_{0.9}\text{Fe}_{0.1}\text{PO}_4$ nanoparticles. Gradually, with the consistence of heating, the glucose begins to dehydrate and polymerize to form glycosides. The color of this mixture turned from yellowish to brown indicating the partial polymerization of the glucose. The polymerization mechanism of glucose was assumed to be similar to the glycosidation of glucose under hydrothermal conditions. The obtained glucose melt-blended LMFP was then treated with hexamethylene diamine(HDA) thereafter and little amounts of HDA was adsorbed on the surface of the partially polymerized glucose. Since HDA has two amidos(– NH_2) per molecule, the other amido in the adsorbed HDA molecule can be used to interact with the following added graphene oxide(GO). Graphene oxide (GO) suspension was prepared by a modified Hummers' method [25,31]. Research showed that amidos have the ability to adsorb on the surface of graphene oxide through electrostatic grafting with epoxy and carboxyl groups in the graphene oxide [33,34]. It should be pointed out that the silicon element originating from silane coupling agent (i.e. APTES) can not be totally removed, which might have a negative effect during the electrochemical performance. In our experiment, compared with the silane coupling agent, the HDA was used as a novel bridging agent for fabricating grapheme-based materials in order to avoid the possible contamination of Si element, since the HDA only contains C, H, O, N which would be easily removed from the system by subsequent calcination.

The trace of amines can be detected by FT-IR measurements as shown in Fig. S2 in the S.I.. After HDA was added, a new peak at 1490 cm^{-1} appears in the FT-IR spectrum of LMFP-P-B sample (HDA treated LMFP). This new peak can be ascribed to the stretching of C–N bonds which may result from the interact of HDA and partially polymerized glucose [35]. After adding GO, the C–N bond would also be observed in the FT-IR spectrum of LMFP-P-C sample (GO encapsulated LMFP). This phenomenon could be ascribed from

either new formed C–N bond or the residual HDA. The new peak shows up at 1700 cm^{-1} corresponding to carboxy groups which confirms the existence of GO in LMFP–P–C sample. Therefore, the $\text{LiMn}_{0.9}\text{Fe}_{0.1}\text{PO}_4$ was successfully connected with GO through the linkage of HDA. The GO capsuled precursor LMFP–P–C was further heated to form the final production of LMFP/C/rGO composite. The thermogravimetry (TG) measurements (Fig. S3 in S.I.) demonstrated the carbon contents of LMFP/C and LMFP/C/rGO were 5%wt and 7%wt respectively, which is much lower than the previously research [31,36–38]. In another word, the thermogravimetry proved although two steps coating was used in our experiment, the relative content of the active material in our research was increasing instead of decreasing without introducing extra carbon.

XRD patterns of LMFP/C and LMFP/C/rGO are shown in Fig. 2, which matched well with the diffraction pattern of the olivine phase of LiMnPO_4 with *Pmnb*(62) space group (JCPDS # 74–0375). It was barely to see the diffraction peaks of the reduced graphene oxide in the LMFP/C/rGO diffraction pattern which might be explain by its small amount compare with the final compound (eg. c.a. 1% wt). Both the diffraction patterns of LMFP/C and LMFP/C/rGO samples showed some slightly shift towards high angle regions with respect to the standard pattern JCPDS # 74–0375. This shift can be attributed to the smaller ion radius of Fe^{2+} (0.92 Å) compared to that of Mn^{2+} (0.97 Å) in our samples. The iron contents, defined as $n_{\text{Fe}}/[(n_{\text{Fe}}+n_{\text{Mn}})] \times 100\%$, in LMFP/C and LMFP/C/rGO were confirmed to be 11% and 10.5% by ICP–AES measurements (Table S1 in S.I.). The composition of our final products can be expressed as $\text{LiMn}_{0.9}\text{Fe}_{0.1}\text{PO}_4$ in short as the deviation is quite small.

Reitveld refinement of XRD patterns were performed using the GSAS package in order to get the lattice parameters of LMFP/C and LMFP/C/rGO (see Fig. S4). The details are listed in Table 1. As can be seen, the reasonable small R_{wp} factors (6.73% for LMFP/C and 7.77% for LMFP/C/rGO respectively) indicate the well synthesized olivine structure with barely any impurity. It is depicted that after the introduced of rGO, the cell volume of $\text{LiMn}_{0.9}\text{Fe}_{0.1}\text{PO}_4$ became larger. This change might be explained as the marginal effect arising from rGO on the crystal structure of $\text{LiMn}_{0.9}\text{Fe}_{0.1}\text{PO}_4$ according to previous research [39].

As it is shown in Fig. 3(a) and (b), a similar morphology of sheet-like aggregates can be observed in both LMFP/C and LMFP/C/rGO

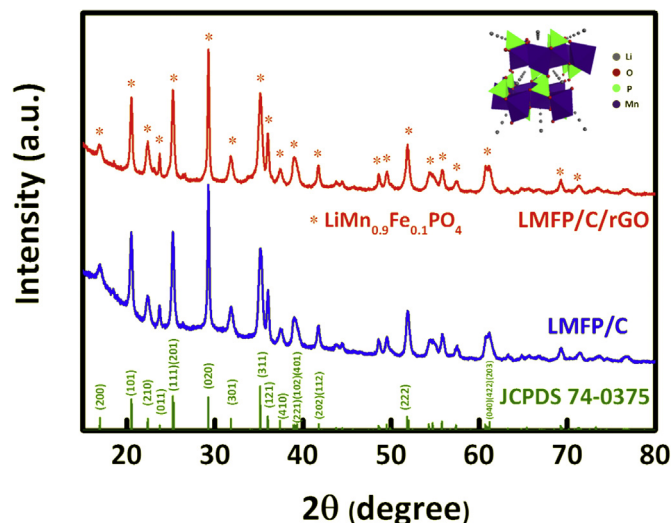


Fig. 2. XRD pattern of LMFP/C/rGO, LMFP/C and JCPDS 74–0375 in red, blue and green respectively. The insert figure shows the corresponding crystal structure of JCPDS 74–0375. (For interpretation of the references to colour in this figure legend, the reader is referred to the web version of this article.)

Table 1
Lattice parameters of the LMFP/C and LMFP/C/rGO samples.

Parameter	A(Å)	b(Å)	c(Å)	V(Å ³)	R _{wp} (%)	R _p	χ ²
LMFP/C	10.437	6.094	4.743	301.669	6.73	5.27	4.906
LMFP/C/rGO	10.445	6.096	4.747	302.254	7.77	5.78	6.561

samples. These nanoparticles have the thickness around 20 nm with the width about 100 nm. For the LMFP/C/rGO, as displayed in Fig. 3(c), crinkled textures which associated with the existence of reduced graphene oxide are dispersed between each LMFP nanoparticles and hence making the particles connected with each other. The connection with graphene provided additional conductive webs which was further confirmed by different magnification of TEM images shown in Fig. 3(c) and (d). The HRTEM image in Fig. 3(d) shows that the $\text{LiMn}_{0.9}\text{Fe}_{0.1}\text{PO}_4$ nanoparticles are uniformly coated by an amorphous carbon layer pyrolyzed using sugar as the carbon source with a thickness around 2 nm and intimately contacted with rGO platelet surfaces. Moreover, the interval width of LMFP nanoparticles can be seen clearly in Fig. 3(c) and (d) with 2.51 Å and 3.02 Å for (131) and (200) respectively. Further analysis showed the BET surface area of LMFP/C and LMFP/C/rGO are 46.7 and 51.4 $\text{m}^2\text{ g}^{-1}$ respectively. The slightly larger surface area of LMFP/C/rGO maybe ascribed to the larger surface area of rGO (see Fig. S5 in S.I.). The small pores (radius less than 15 nm) of the samples may result from the amorphous carbon on the surface of $\text{LiMn}_{0.9}\text{Fe}_{0.1}\text{PO}_4$ nanoparticles and the mesopores with the pore radius in the range of 15–60 nm were attributed from the spaces between particles. The large interval space within LMFP/C/rGO particles facilitates the electrolyte penetration and leads to the better rate performance of LMFP/C/rGO which can be seen in the electrochemical performance (See Fig. S5 in S.I.).

The initial three cycles charge–discharge curves of LMFP/C/rGO is shown in Fig. 4(a). The cell was first charged at a constant current of 0.1C ($1\text{C} = 170\text{ mA g}^{-1}$, based on the total mass of LMFP/C or LMFP/C/rGO) within a voltage range from 2.0 V to 4.5 V, then followed by a constant voltage of 4.5 V for 1 h in order to fully delithiated the electrode. The electrochemical tests showed the first charge and discharge capacity of LMFP/C/rGO is 195 and 158 mAh g^{-1} respectively. The coulombic efficiency at initial cycle for LMFP/C/rGO is relatively low which could be attributed to the decomposition of the electrolyte, whereas this efficiency gradually raised up from the second cycle and exceed 95% at the third cycle which indicates a stable solid–electrolyte interface (SEI) formation. The bend curves observed between 3.4 V and 3.7 V (v.s. Li^+/Li) could be ascribed to the redox reaction of $\text{Fe}^{2+} \leftrightarrow \text{Fe}^{3+}$ upon cycling that is a characteristic redox plateau of Fe^{2+} in the olivine-structured $\text{LiMn}_{0.9}\text{Fe}_{0.1}\text{PO}_4$ [18]. Within the 3.9 V and 4.3 V range, the LMFP/C/rGO cathode showed a clear redox potential plateau around 4.15 V (for charge) and 4.05 V (for discharge), which corresponding to the $\text{Mn}^{2+} \leftrightarrow \text{Mn}^{3+}$, the main redox reaction of LMFP/C/rGO during electrochemical process [31,32] which delivered a capacity of more than 120 mAh g^{-1} . The two redox reaction pairs are further confirmed by the cyclic voltammetry measurement as can be seen in Fig. S6. Two pairs of redox waves in the potential range of 3.4 V–3.7 V and 3.9 V–4.3 V are referred to the $\text{Fe}^{2+}/\text{Fe}^{3+}$ and $\text{Mn}^{2+}/\text{Mn}^{3+}$ respectively.

The comparison study of rate performance for LMFP/C and LMFP/C/rGO were also performed which can be found in Fig. 4(b). (The corresponding discharge profiles are depicted in Fig. 4(c) and (d)). It can be seen in Fig. 4(b) that the discharge capacities of the LMFP/C at 0.1C and 2C rates are 161.2 mAh g^{-1} , 130.4 mAh g^{-1} (80.9% retention) respectively, while those capacities for the LMFP/C/rGO are 158.0 mAh g^{-1} and 145.1 mAh g^{-1} (93.6% retention).

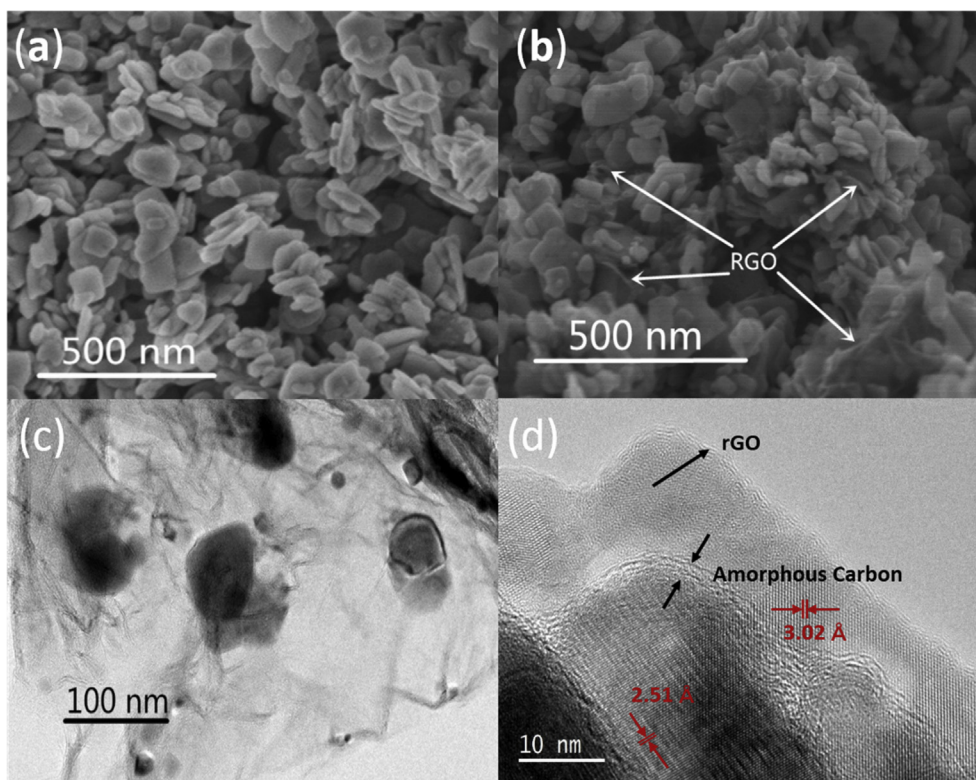


Fig. 3. SEM figure of (a) LMFP/C sample synthesized without adding ascorbic acid in solvothermal process. (b) LMFP/C/rGO sample synthesized with adding ascorbic acid. (c–d) TEM figures of LMFP/C/rGO with different magnification.

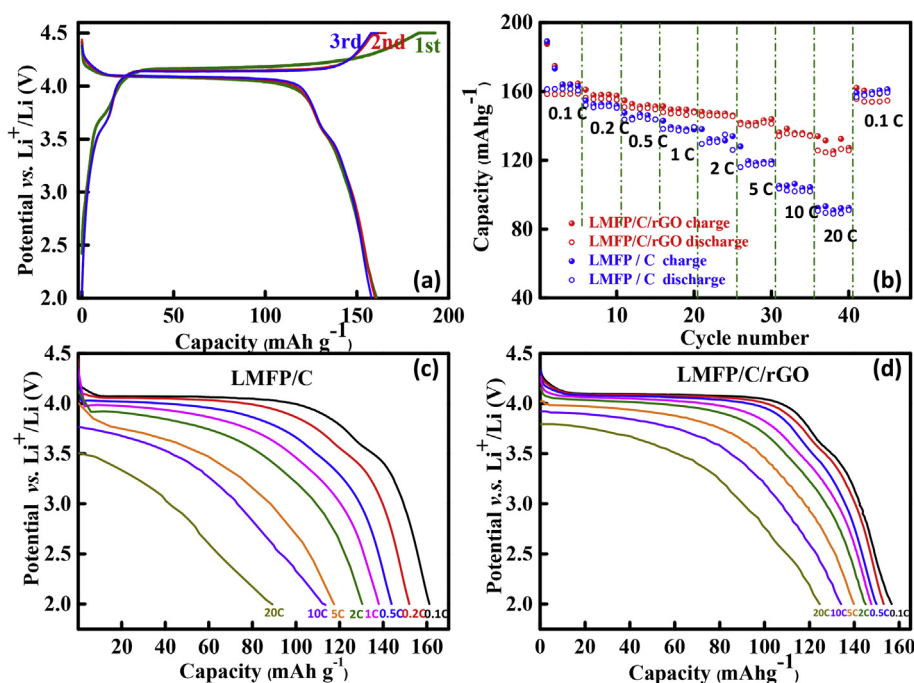


Fig. 4. Electrochemical test of (a) charge/discharge curves of LMFP/C/rGO electrode at the current density of 0.1 C (b) rate performance of LMFP/C and LMFP/C/rGO from 0.1 C to 20 C and discharge curves of (c) LMFP/C and (d) LMFP/C/rGO at different current densities.

Moreover, the rate performance at 20C showed the LMFP/C/rGO delivering a specific capacity of 124.6 mAh g^{-1} which is far better than the single amorphous carbon coating LMFP/C (89.2 mAh g^{-1}). The electrochemical tests demonstrated unambiguously the

advantage of our elaborate design of hierarchical bridge like two steps carbon coating. Although the capacity of LMFP/C is slightly higher than LMFP/C/rGO at the low rate (0.1C), LMFP/C/rGO shows much better capacity retention during charging and discharging at

higher current density. Specifically, as it is depicted in Fig. 4(c) and (d) the overpotential of LMFP/C/rGO at high rates is significantly smaller than that of LMFP/C. For instance, the average discharge potential of LMFP/C/rGO at 20C rate is 3.5 V while for the LMFP/C this value is lower than 3.0 V. This difference of overpotential refers to the inherent polarization and can be ascribed to the improvement of C/rGO two steps coating that will be further discussed below.

In order to clarify the impact of rGO in the LMFP/C/rGO electrode, especially at high discharge current densities, both LMFP/C and LMFP/C/rGO electrode were subjected to electrochemical impedance spectroscopy (EIS) measurements. Fig. 5 shows the EIS measurements of two electrodes with the same depth of discharge (DOD = 50%). As shown in Fig. 5, the EIS plots of each electrode consist of semicircles in the high and medium frequencies with the inclined line in the lower frequency region. The LMFP/C/rGO semicircle in the high frequent region, which associated with the charge transfer resistant (R_{ct}), is significant smaller than that of LMFP/C. To quantitatively identify the influence, the EIS plots are fitted using the equivalent circuit model (see insert part of Fig. 5). In the equivalent circuit, R_3 represent Ohmic resistance of two electrodes while R_1 (which is often symbolled as R_{ct}) and R_2 represent charge transfer resistance and surface resistance respectively. The fitting results, listed in Support information (Table S2), disclosed that the Ohmic resistances of LMFP/C and LMFP/C/rGO electrode are 8.347 and 8.286 Ω respectively. Follow the same order, the charge transfer resistance of LMFP/C/rGO is 12.47 Ω which is much lower than that of LMFP/C as 48.86 Ohm. This phenomenon may be related to the higher electric conduction of LMFP/C/rGO compared to LMFP/C. Such smaller charge transfer and Ohmic resistance is one of the key factors contributed for the excellent electrochemical performance of LMFP/C/rGO, especially for the rate performance.

The cycling capability of LMFP/C and LMFP/C/rGO were tested at a current density of 0.2C after the rate performance test. The results are depicted in Fig. 6. After 140 cycles of charge/discharge the capacity retention of LMFP/C/rGO electrode is 95% which is superior to the 90% retention of LMFP/C (Fig. S7). The enhancement of cycling stability could attribute to the highly stable contact of active materials ($\text{LiMn}_{0.9}\text{Fe}_{0.1}\text{PO}_4$) with the current collector and carbon source through the three dimensional conductive network. Meanwhile higher surface area and larger porosity of LMFP/C/rGO facilitate the electrolyte transportation to the LMFP particles compared with LMFP/C.

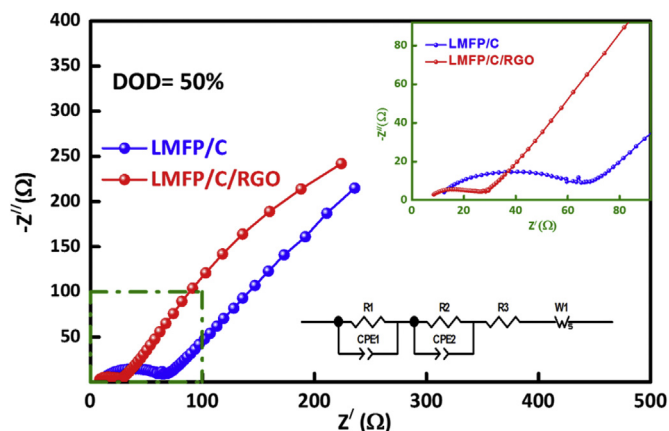


Fig. 5. The Nyquist plot of LMFP/C and LMFP/C/rGO electrode tested at 50% state of discharge depth in the frequency range of 10^5 – 10^{-2} Hz followed by the rate performance tests. The insert plot shows the equivalent circuit (bottom part) and the magnification of the EIS plots (up part) at high and medium frequencies.

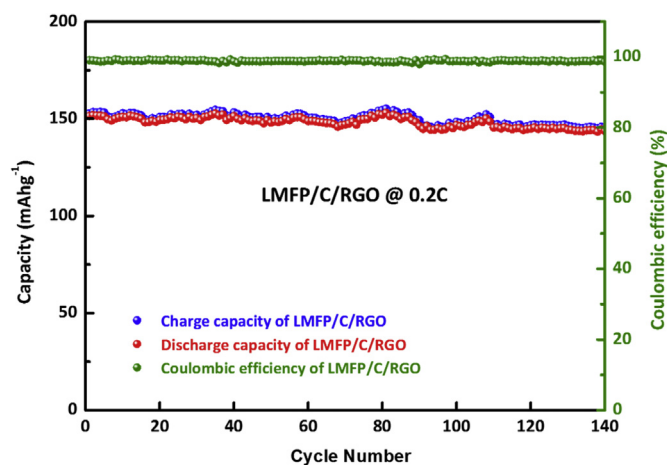


Fig. 6. Cycling performances of LMFP/C/rGO at a current density of 0.2 C.

4. Conclusion

In summary, an amorphous carbon and reduced graphene oxide co-doped $\text{LiMn}_{0.9}\text{Fe}_{0.1}\text{PO}_4$ (LMFP/C/rGO) is synthesized by a novel amine-assisted method. For comparison, the $\text{LiMn}_{0.9}\text{Fe}_{0.1}\text{PO}_4$ with only pyrolyzed carbon coating (LMFP/C) is also prepared. The final products are characterized by XRD which confirmed the synthesized materials are well designed olivine-structured materials. For the LMFP/C/rGO sample, plate-like $\text{LiMn}_{0.9}\text{Fe}_{0.1}\text{PO}_4$ nanoparticles are adsorbed on the surface of rGO sheets with superior electronic conductivity. The average particle size of $\text{LiMn}_{0.9}\text{Fe}_{0.1}\text{PO}_4$ is in nanoscale with the thickness less than 20 nm and the thickness of amorphous carbon coating layer is c.a. 2 nm. Remarkably, the LMFP/C/rGO shows a high initial capacity (158.0 mAh g^{-1}) at the low current density (0.1C) and exhibits excellent capacity retention (80.4%) at a high current density of 20C. After 140 cycles at 0.2C, 95% capacity retention is still achieved. The excellent electrochemical performance of the LMFP/C/rGO could be attributed to the successfully synthesis of the hierarchical and bridging LMFP/C/rGO structure that ensures a uniform coating of the amorphous carbon linked closely with the high electric conducting of rGO. Our results showed the novel two steps carbon coated $\text{LiMn}_{0.9}\text{Fe}_{0.1}\text{PO}_4$ can be used as a promising cathode material for Li-ion battery with high electronic and ionic conductivity. Moreover, this effective novel synthesis strategy can be extended and widely used in the structure morphology for advanced energy storage application.

Acknowledgements

This research was partially supported financially by The National Key Research and Development Program of China (2016YFB0100203), National Natural Science Foundation of China (21673116, 21403107, 21373111, 51602144), Natural Science Foundation of Jiangsu Province of China (BK20140055, BK20160068), PAPD of Jiangsu Higher Education Institutions, and the Project on Union of Industry-Study-Research of Jiangsu Province (BY2015069-01).

Appendix A. Supplementary data

Supplementary data related to this article can be found at <http://dx.doi.org/10.1016/j.jpowsour.2017.05.067>.

References

- [1] A.K. Padhi, K.S. Nanjundaswamy, J.B. Goodenough, *J. Electrochem. Soc.* 144 (1997) 1188–1194.
- [2] L. Yuan, Z. Wang, W. Zhang, X. Hu, J. Chen, Y. Huang, *J. Goodenough, Energy Environ. Sci.* 4 (2011) 269–284.
- [3] H. Yoo, M. Jo, B. Jin, H. Kim, J. Cho, *Adv. Energy. Mater* 1 (2011) 347–351.
- [4] H. Huang, S. Yin, L.F. Nazar, *Electrochem. Solid State Lett.* 4 (2001) A170–A172.
- [5] Y.G. Wang, P. He, H.S. Zhou, *Energy Environ. Sci.* 4 (2011) 805–817.
- [6] H. Guo, C. Wu, J. Xie, S. Zhang, G. Cao, X. Zhao, *J. Mater. Chem. A* 2 (2014) 10581–10588.
- [7] P. He, X. Zhang, Y.G. Wang, L. Cheng, Y.Y. Xia, *J. Electrochem. Soc.* 155 (2008) A144–A150.
- [8] J. Goodenough, Y. Kim, *Chem. Mater* 22 (2010) 587–603.
- [9] Y.Y. Cai, D.Y. Zhang, C.K. Chang, Z.M. Sheng, K.J. Huang, *Ionics* 22 (2016) 1011–1019.
- [10] P. He, J.L. Liu, W.J. Cui, J.Y. Luo, Y.Y. Xia, *Electrochimica Acta* 56 (2011) 2351–2357.
- [11] C. Delacourt, L. Laffont, R. Bouchet, C. Wurm, J. Leriche, M. Morcrette, J. Tarascon, C. Masquelier, *J. Electrochem. Soc.* 152 (2005) A913–A921.
- [12] T.-H. Kim, H.-S. Park, M.-H. Lee, S.-Y. Lee, H.-K. Song, *J. Power Sources* 210 (2012) 1–6.
- [13] D. Morgan, A. Van der Ven, G. Cere, *Electrochem. Solid State Lett.* 7 (2004) A30–A32.
- [14] A. Yamada, S. Chung, *J. Electrochem. Soc.* 148 (2001) A960–A967.
- [15] D. Choi, J. Xiao, Y.J. Choi, J.S. Hardy, M. Vijayakumar, M.S. Bhuvaneshwari, J. Liu, W. Xu, W. Wang, Z.G. Yang, G.L. Graff, J.G. Zhang, *Energy Environ. Sci.* 4 (2011) 4560–4566.
- [16] S.L. Yang, R.G. Ma, M.J. Hu, L. Xi, Z.G. Lu, C.Y. Chung, *J. Mater. Chem.* 22 (2012) 25402–25408.
- [17] X. Rui, X. Zhao, Z. Lu, H. Tan, D. Sim, H. Hng, R. Yazami, T. Lim, Q. Yan, *ACS Nano* 7 (2013) 5637–5646.
- [18] Y. Hong, Z.L. Tang, Z.J. Hong, Z.T. Zhang, *J. Power Sources* 248 (2014) 655–659.
- [19] H.-C. Dinh, S.-L. Mho, I.-H. Yeo, Y. Kang, D.-W. Kim, *RSC Adv.* 5 (2015) 100709–100714.
- [20] Y.Z. Dong, H. Xie, J. Song, M.W. Xu, Y.M. Zhao, J.B. Goodenough, *J. Electrochem. Soc.* 159 (2012) A995–A998.
- [21] C.L. Hu, H.H. Yi, H.S. Fang, B. Yan, Y.C. Yao, W.H. Ma, Y.N. Dai, *Electrochem. Commun.* 12 (2010) 1784–1787.
- [22] P.J. Zuo, G.Y. Cheng, L.G. Wang, Y.L. Ma, C.Y. Du, X.Q. Cheng, Z.B. Wang, G.P. Yin, *J. Power Sources* 243 (2013) 872–879.
- [23] J. Ni, L. Gao, *J. Power Sources* 196 (2011) 6498–6501.
- [24] R. Malik, F. Zhou, G. Ceder, *Phys. Rev. B* 79 (2009) 214201.
- [25] H.L. Wang, Y. Yang, Y.Y. Liang, L.F. Cui, H.S. Casalongue, Y.G. Li, G.S. Hong, Y. Cui, H. Dai, *Angew. Chem. Int. Ed.* 50 (2011) 7364–7368.
- [26] K.M. Jense, M. Christensen, H.P. Gunnlaugsson, N. Lock, E.D. Bojesen, T. Proffen, B. Iversen, *Chem. Mater* 25 (2013) 2282–2290.
- [27] Y.-K. Sun, S.-M. Oh, H.-K. Park, B. Scrosati, *Adv. Mater* 23 (2011) 5050–5054.
- [28] Y.G. Wang, Y.R. Wang, E. Hosono, K.X. Wang, H.S. Zhou, *Angew. Chem. Int. Ed.* 47 (2008) 7461–7465.
- [29] Y.Y. Mi, P. Gao, W. Liu, W.D. Zhang, H.H. Zhou, *J. Power Sources* 267 (2014) 459–468.
- [30] K. Kagesawa, E. Hosono, M. Okubo, K. Kikkawa, D. Hamane, T. Kudo, H.S. Zhou, *CrysEngComm* 15 (2013) 6638–6640.
- [31] J. Zong, X.J. Liu, *Electrochimica Acta* 116 (2014) 9–18.
- [32] K. Wang, Y.G. Wang, C.X. Wang, Y.Y. Xia, *Electrochimica Acta* 146 (2014) 8–14.
- [33] Z.M. Zheng, Y.L. Cheng, X.B. Yan, R.T. Wang, P. Zhang, *J. Mater. Chem. A* 2 (2014) 149–154.
- [34] K. Zhang, J.T. Lee, P. Li, B. Kang, J.H. Kim, G.R. Yi, J.H. Park, *Nano Lett.* 15 (2015) 6756–6763.
- [35] W.W. Zhou, J.X. Zhu, C.W. Cheng, J.P. Liu, H.P. Yang, C.X. Cong, C. Guang, X.T. Jia, H.J. Fan, Q.Y. Yan, C. Li, T. Yu, *Energy Environ. Sci.* 4 (2011) 4954–4961.
- [36] X. Hu, X. Sun, M. Yang, H. Ji, X. Li, S. Cai, R. Guo, F. Hou, C. Zheng, W. Hu, *J. Mater. Chem.* 52 (2017) 3597–3612.
- [37] Z. Wu, Y. Long, X. Lv, J. Su, Y. Wen, *Ceram. Int.* 43 (2017) 6089–6095.
- [38] S. Liu, H. Fang, E. Dai, B. Yang, Y. Yao, W. Ma, Y. Dai, *Electrochimica Acta* 116 (2014) 97–102.
- [39] H. Xu, J. Zong, F. Ding, Z.W. Lu, W. Li, X.J. Liu, *RSC Adv.* 6 (2016) 27164–27169.